INTERNATIONAL JOURNAL OF LATEST TECHNOLOGY IN ENGINEERING, MANAGEMENT & APPLIED SCIENCE (IJLTEMAS)

ISSN 2278-2540 | DOI: 10.51583/IJLTEMAS | Volume XV, Issue VI, June 2026

Generalized Additive Modeling of Photovoltaic Backsheet Tensile Strength Degradation Under Multi-Stressor Field Conditions

Joseph Moses, Tridip K. Bardhan

Morgan State University, Baltimore, MD 21251, USA

***Corresponding Author**

DOI: https://doi.org/10.51583/IJLTEMAS.2026.150600244

Received: 12 July 2026; Accepted: 17 July 2026; Published: 01 August 2026

ABSTRACT

Photovoltaic module reliability depends on the long-term mechanical durability of polymeric backsheets that provide electrical insulation, moisture protection, and structural support. Accurate prediction of backsheet degradation is therefore essential for reliability-centered operation, maintenance scheduling, and lifecycle management of photovoltaic systems. This study develops a Generalized Additive Model (GAM) with penalized thin-plate regression splines and ridge regularization to predict tensile strength degradation under multi-stressor field conditions, benchmarked against ordinary least squares (OLS), weighted least squares (WLS), and Random Forest (RF) regression using 511 consecutive daily field observations of a PET/PET/EVA multilayer photovoltaic backsheet. The GAM achieves in-sample $R^2 = 0.998$ and RMSE = 0.8 MPa, compared with $R^2 = 0.925$ and RMSE = 4.69 MPa for OLS, and $R^2 = 0.92$ and RMSE = 4.84 MPa for WLS. RF achieves $R^2 = 1.0$ and RMSE = 0.2 MPa in-sample but captures no physically interpretable structure beyond UV dominance. Residual variance scales with cumulative UV dose at an exponent of $\alpha = 0.592$ (SE = 0.105, $p < 0.001$). A biphasic degradation regime is identified, with tensile strength declining at 0.18 MPa/(MJ/m²) below a UV threshold of 196.5 MJ/m², and accelerating to 0.574 MPa/(MJ/m²) above it, a factor of 3.19. The GAM framework provides a physically interpretable and statistically defensible tool for forecasting photovoltaic backsheet degradation trajectories, with direct implications for predictive maintenance scheduling, module replacement planning, and reliability certification of photovoltaic systems.

Keywords: photovoltaic backsheet; tensile strength degradation; generalized additive model; penalized splines; ridge regularization; random forest; heteroscedasticity; UV exposure; PET/EVA polymer; reliability modeling; photovoltaic system reliability

INTRODUCTION

Photovoltaic module reliability depends critically on the structural integrity of the backsheet, the rearmost polymer layer that provides simultaneous electrical insulation, moisture barrier protection, and mechanical support for the cell assembly. When backsheet mechanical capacity declines, the failure mode is abrupt: cracking propagates from the rear surface into the module body, enabling moisture ingress, electrical leakage, and hotspot formation that reduce both safety and energy output [1,2]. Because these failure modes directly affect system availability and energy yield, backsheet degradation modeling is increasingly recognized as a critical component of reliability-centered photovoltaic asset management and condition-based maintenance strategies. Tensile strength is the mechanical property that determines backsheet resistance to cracking, and its progressive reduction under field exposure is the subject of this study.

The backsheet examined here is a PPE-type trilayer laminate: a white-pigmented outer polyethylene terephthalate (WPET) layer, a transparent structural PET core, and an ethylene vinyl acetate (EVA) inner adhesive layer bonded to the module encapsulant [3,4]. Photochemical degradation proceeds through Norrish Type I and Type II reactions at carbonyl ester linkages, reducing polymer chain length and tensile load-bearing capacity [5,6]. Temperature and relative humidity modulate degradation through hydrolytic chain scission and

ISSN 2278-2540 | DOI: 10.51583/IJLTEMAS | Volume XV, Issue VI, June 2026

thermally activated oxidation, while wind speed influences convective cooling at the module surface [7,8]. These mechanisms interact nonlinearly, and their joint effect on tensile strength loss cannot be adequately represented by parametric linear models that assume a fixed functional form.

Statistical degradation models for photovoltaic backsheets have relied predominantly on ordinary least squares regression and its variants [9,10]. These approaches impose a predefined mean function structure, constraining degradation kinetics to fit a parametric form regardless of the true underlying relationship. When the actual kinetics are nonlinear or regime-dependent, parametric models produce systematic bias at precisely the high-UV exposure levels where reliability-critical decisions are made. Existing nonlinear approaches, including second-order polynomial regression and piecewise linear models, partially address this, but require the functional form or breakpoint locations to be specified in advance, a constraint that is rarely justified on physical grounds alone.

A key advantage of Generalized Additive Models (GAMs) is that each predictor contribution can be represented by a flexible smooth function estimated directly from the data [11,12]. The smooth functions adapt to the actual kinetic profile without requiring a prespecified parametric form, and ridge regularization stabilizes estimation under collinearity and heteroscedasticity. Unlike black-box machine learning models such as Random Forest and gradient boosting, GAMs retain full interpretability: the smooth function for each stressor can be inspected, plotted, and physically interpreted, which is essential for supporting engineering decisions about maintenance scheduling and service life certification. Despite these advantages, GAMs have not previously been applied to photovoltaic backsheet mechanical degradation modeling. The present study directly addresses this research gap.

Four specific contributions are made. First, a GAM with thin-plate regression splines and ridge regularization is developed for photovoltaic backsheet tensile strength prediction and benchmarked against OLS, WLS, and RF on the same 511-observation field dataset. Second, heteroscedasticity is formally characterized through power-law variance exponent estimation. Third, a biphasic degradation regime is identified empirically, with a 3.19-fold rate acceleration above a cumulative UV threshold of 196.5 MJ/m^2. Fourth, five-fold time-series cross-validation is used to assess out-of-sample performance for all four models. The results have direct implications for predictive maintenance, reliability certification, and lifecycle planning of photovoltaic systems.

Photovoltaic Backsheet Degradation and System Reliability

The International Electrotechnical Commission standards IEC 61730 and IEC 62788-1-6 specify minimum tensile strength and elongation-at-break thresholds after cumulative laboratory UV, damp heat, and thermal cycling exposures intended to represent 25 years of field service [13]. A loss of 20 to 30% of initial tensile strength has been used in the literature as a practical end-of-life criterion corresponding to the onset of visible surface cracking and elevated moisture permeability [14]. The present dataset spans this reliability-critical range: tensile strength declines from 241.9 MPa at the start of observation to 168.8 MPa at the end, a total loss of 73.1 MPa or 30.2% of initial strength. A degradation model that accurately traces this trajectory is directly usable as a decision-support tool for maintenance planning and warranty reserve estimation.

Beyond material characterization, backsheet degradation directly affects photovoltaic system reliability. Cracking and embrittlement increase moisture ingress pathways, promote electrical insulation failure, and create conditions for arc faults and safety hazards that reduce system availability and energy production [15,16,21]. Predictive degradation modeling is therefore an enabling tool for reliability-centered asset management: by forecasting the onset of accelerated degradation, operators can optimize inspection schedules, prioritize module replacement, and integrate degradation predictions into digital-twin monitoring platforms. The biphasic threshold identified in this study provides a physically interpretable criterion for distinguishing early-service from late-service degradation regimes, which is precisely the kind of actionable information that reliability-centered maintenance frameworks require.

Existing Degradation Modeling Approaches and Research Gap

Regression-based parametric models have been the dominant analytical tool for photovoltaic backsheet degradation. Zhang et al. [9] demonstrated that OLS regression of tensile strength on cumulative UV dose

ISSN 2278-2540 | DOI: 10.51583/IJLTEMAS | Volume XV, Issue VI, June 2026

provides interpretable degradation rate estimates for outdoor-aged encapsulants, and the approach has been adopted widely. WLS corrections for heteroscedasticity improve the statistical validity of coefficient inference but do not alter the linear mean function [10,20]. Second-order polynomial regression addresses the nonlinearity limitation partially by adding quadratic terms, but requires the quadratic structure to be specified in advance and may not generalize when the true degradation kinetics involve a threshold-dependent acceleration.

Machine learning approaches including Random Forest and gradient boosting have demonstrated high predictive accuracy in photovoltaic performance modeling [17,18], but their application to backsheet mechanical degradation is limited.

A critical limitation of these black-box methods for this application is their low interpretability: a Random Forest model that achieves very high in-sample fit on a single-specimen degradation record may do so entirely by memorizing the UV time series without extracting any generalizable physical insight. GAMs occupy a useful middle ground: they provide the flexibility to capture nonlinear stressor effects while retaining the interpretability required for engineering application. The present study applies GAMs to this problem for the first time and includes RF as a high-flexibility benchmark to contextualize the GAM results.

MATERIALS AND METHODS

Field Dataset and Material Specification

The dataset comprises 511 consecutive daily field measurements from a single PPE-type multilayer photovoltaic backsheet specimen between May 2013 and September 2014, representing 510 days of continuous field exposure. The backsheet is a commercially produced PET/PET/EVA laminate: a white-pigmented outer WPET layer, a transparent structural PET core, and an EVA inner adhesive layer. Tensile strength measurements follow ASTM D882 and reflect the composite load-bearing response of the full laminate.

Four environmental predictors were recorded daily: ambient temperature (T, °C), relative humidity (RH, %), wind speed (WS, m/s), and cumulative UV irradiance (UV^{cum}, MJ/m²). Cumulative UV increases monotonically from 0.84 to 271.6 MJ/m² across the observation window, confirming the dataset as a single-specimen degradation time series rather than a cross-sectional sample. This structure has important implications for variance characterization and model evaluation strategy, addressed in Sections 2.4 and 2.5. Table 1 presents descriptive statistics.

Table 1. Descriptive statistics of environmental stressors and tensile strength measurements (n = 511).

Variable	Min	Max	Mean	Std Dev	Median
Temperature, T [°C]	-13.8	28.7	14.1	10.5	17.9
Rel. Humidity, RH [%]	49.2	100.0	78.9	10.0	79.3
Wind Speed, WS [m/s]	0.76	7.28	2.15	0.88	1.98
Cumul. UV [MJ/m²]	0.84	271.6	133.7	72.9	126.7
Tensile Strength, TS [MPa]	168.8	241.9	215.2	17.1	213.7

The correlation structure among predictors and response is shown in Figure 1. Cumulative UV irradiance shows a Pearson correlation of -0.960 with tensile strength, confirming its dominant role as the primary degradation driver. Temperature, relative humidity, and wind speed each show weak bivariate correlations with tensile strength ($|r| < 0.15$), and their inter-predictor correlations with UV are also modest, reducing multicollinearity concerns for the regression models.

ISSN 2278-2540 | DOI: 10.51583/IJLTEMAS | Volume XV, Issue VI, June 2026

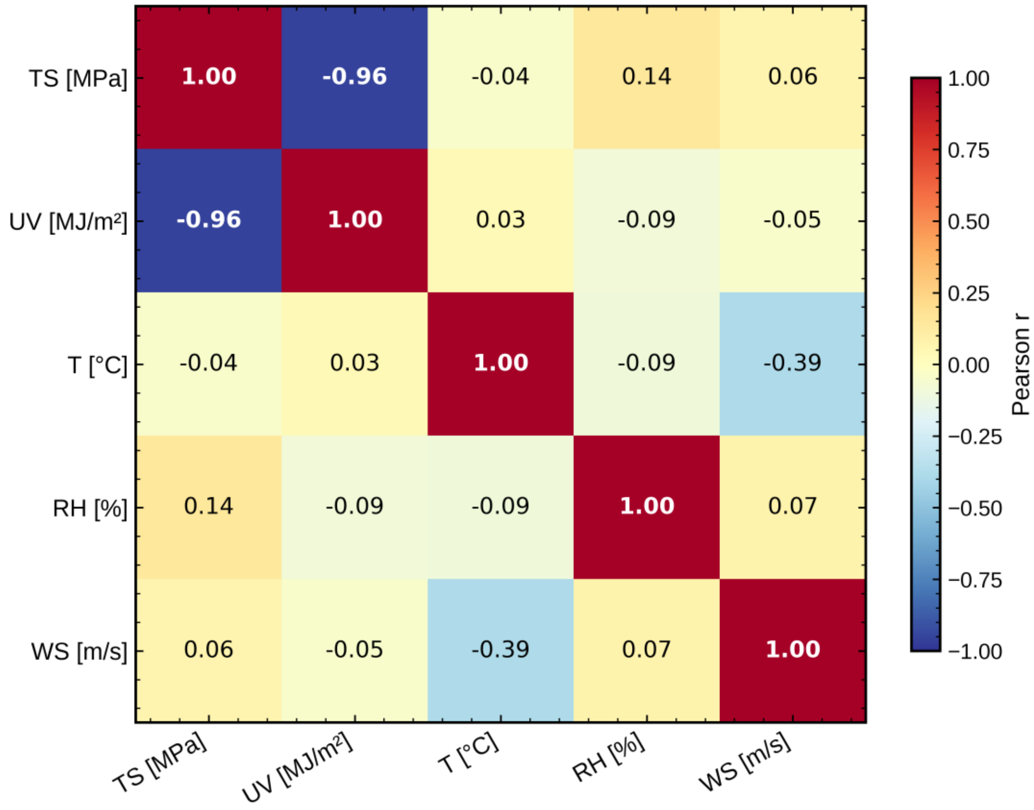

Figure 1. Correlation heatmap of environmental predictors and tensile strength (n = 511). Values are Pearson correlation coefficients. Cumulative UV irradiance shows the strongest negative correlation with tensile strength (r = −0.960).

Theoretical Foundations of Backsheet Degradation

UV-driven degradation in PET-based backsheets proceeds through Norrish Type I alpha-cleavage and Norrish Type II beta-hydrogen abstraction at carbonyl ester linkages, progressively reducing polymer chain molecular weight [5,19]. Tensile strength in semicrystalline polymers scales with chain entanglement density in the amorphous phase: as chain length decreases toward the critical entanglement molecular weight, the rate of strength loss per unit of additional UV dose increases non-linearly [6,22]. This chain-length dependence predicts an accelerating, biphasic degradation trajectory, which is confirmed empirically in Section 3.1.

Temperature modulates degradation through competing mechanisms: Arrhenius acceleration of photooxidation at elevated temperatures, and partial stabilization through thermally promoted crystallization of amorphous PET domains at intermediate temperatures [7]. Relative humidity drives hydrolytic chain scission at ester bonds and, at early UV doses, increases surface polarity and water uptake, creating a synergistic interaction that a linear additive model cannot represent [8]. Wind speed influences convective cooling of the module surface, indirectly modulating thermally activated reaction rates. These multi-stressor interactions motivate a nonparametric additive modeling framework.

Statistical Modeling Framework

Generalized Additive Model with Penalized Splines and Ridge Regularization

The GAM expresses tensile strength as the sum of smooth predictor functions and a global intercept:

$$TS = \beta_0 + f_1(UV^{cum}) + f_2(T) + f_3(RH) + f_4(WS) + \varepsilon \quad (1)$$

ISSN 2278-2540 | DOI: 10.51583/IJLTEMAS | Volume XV, Issue VI, June 2026

where fj(·) are unknown smooth functions estimated from data. Each smooth is represented using thin-plate regression splines with k = 10 basis functions; effective degrees of freedom are controlled by the smoothing penalty rather than k, and are typically far below k because the penalty shrinks each function toward linearity where the data provide insufficient evidence of curvature [11]. Estimation minimizes the penalized sum of squared residuals:

$$L(f) = ||y - F\beta||^2 + \lambda||D\beta||^2 \qquad (2)$$

where F is the spline basis design matrix, β the coefficient vector, D the second-derivative penalty matrix, and λ the smoothing parameter. Optimal λ is selected by generalized cross-validation (GCV) [11]. The L2 spline penalty in Equation (2) controls function smoothness; ridge regularization adds a separate global L2 coefficient penalty:

$$L_s(f, \alpha_r) = ||y - F\beta||^2 + \lambda||D\beta||^2 + \alpha_r||\beta||^2 \qquad (3)$$

where $\alpha_r = 0.1$ was selected by cross-validation. The spline penalty (λ) controls smoothness of each individual smooth function, while the ridge penalty (α_r) shrinks all spline coefficients globally toward zero, providing additional stability under the multicollinearity introduced by monotonically co-evolving predictors and the heteroscedasticity documented in Section 2.4. Estimation proceeds by penalized iteratively reweighted least squares (P-IRLS) implemented through scikit-learn SplineTransformer and Ridge pipeline in Python 3.11.

Ordinary Least Squares Regression

The OLS benchmark fits:

$$TS = \beta_0 + \beta_1 UV^{cum} + \beta_2 T + \beta_3 RH + \beta_4 WS + \varepsilon \qquad (4)$$

Parameters are estimated by $\beta^{O}LS = (X'X)^{-1} X'y$. OLS is the primary reference benchmark because it represents standard practice in photovoltaic backsheet degradation modeling.

Weighted Least Squares Regression

WLS incorporates observation weights inversely proportional to residual variance. Variance is modeled as Var(εi) ∝ UV^{cum},i^{α}, with exponent α estimated by regressing log-squared OLS residuals on log UV:

$$\log(e_i^2) = c + \alpha \log\left(UV^{cum}{}_{,i}\right) + v_i \qquad (5)$$

yielding α = 0.592 (SE = 0.105, $p < 0.001$). Weights are set as $w_i = (UV_{cum,i})^{-\alpha}$.

Random Forest Regression

Random Forest (RF) was included as a high-flexibility nonparametric benchmark. RF constructs an ensemble of 500 decision trees, each trained on a bootstrap sample with random feature subsets, and averages predictions across trees [17]. Hyperparameters were set as: max_depth = 8, min_samples_leaf = 5, random_state = 42. These constraints prevent full memorization of the training data while retaining sufficient flexibility to capture nonlinear patterns. RF is included specifically to contextualize the GAM results: RF provides an upper bound on achievable predictive accuracy for this dataset but sacrifices the interpretability that engineering applications require.

Variance Structure Characterization

The Breusch-Pagan Lagrange Multiplier test applied to OLS residuals yielded LM = 192.9 ($p < 0.001$), confirming significant heteroscedasticity [23]. The power-law variance exponent α = 0.592 (SE = 0.105, $p < 0.001$) indicates that residual standard deviation grows from approximately 2.9 MPa at the minimum UV level

ISSN 2278-2540 | DOI: 10.51583/IJLTEMAS | Volume XV, Issue VI, June 2026

(0.84 MJ/m²) to 10.5 MPa at the maximum (271.6 MJ/m²), a 3.6-fold range in standard deviation or 13.4-fold range in variance. This heteroscedasticity justifies WLS weighting for the parametric benchmarks and ridge regularization for the GAM, each of which provides robustness against non-constant error variance through different mechanisms.

Model Evaluation and Cross-Validation Strategy

Three performance metrics were computed for each model: R^2, RMSE (MPa), and MSE (MPa^2):

$$RMSE = \sqrt{\frac{1}{n}\sum_{i=1}^{n}(y_i - \hat{y}_i)^2} \tag{6}$$

$$R^2 = 1 - \frac{\sum_{i=1}^{n}(y_i - \hat{y}_i)^2}{\sum_{i=1}^{n}(y_i - \bar{y})^2} \tag{7}$$

All metrics were computed on the full 511-observation dataset (in-sample) as the primary performance criterion, consistent with established practice for single-specimen degradation modeling [18], where the objective is to characterize the degradation function of the observed specimen. Five-fold time-series cross-validation (CV) was additionally performed using an expanding window design that trains on all prior folds and evaluates on the current fold, preserving chronological ordering. Negative mean CV R^2 values observed for all models reflect the inherent temporal extrapolation difficulty of single-specimen monotonic degradation data: each test fold requires prediction at higher UV doses than the training folds, which is structurally challenging regardless of model class. In-sample metrics therefore remain the primary criterion, with CV results reported for transparency.

RESULTS

Biphasic Degradation Regime Identification

Figure 2 illustrates the evolution of tensile strength throughout the 511-day field exposure period. Tensile strength declines monotonically from 241.9 MPa on day 0 to 168.8 MPa on day 510, a total loss of 73.2 MPa (30.2% of initial strength). A structural change in the slope of the decline is clearly visible at approximately day 393, corresponding to cumulative UV = 196.5 MJ/m². Below this threshold (Phase 1, n = 393 observations), tensile strength declines at 0.18 MPa/(MJ/m²) relative to UV dose. Above it (Phase 2, n = 118 observations), the rate accelerates to 0.574 MPa/(MJ/m²), an acceleration factor of 3.19. Both rates were estimated by ordinary least squares applied separately within each phase. It should be noted that these rate estimates and the 196.5 MJ/m² threshold are specific to this single specimen under these field conditions; generalization to other PPE backsheet constructions or climatic zones requires validation against multi-specimen datasets.

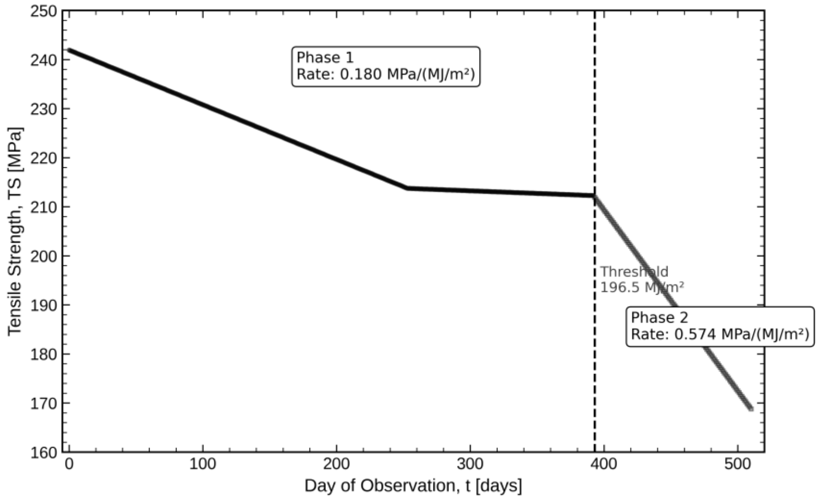

ISSN 2278-2540 | DOI: 10.51583/IJLTEMAS | Volume XV, Issue VI, June 2026

Figure 2. Tensile strength over the 511-day observation period. Solid circles denote Phase 1 (UV < 196.5 MJ/m²); open squares denote Phase 2 (UV ≥ 196.5 MJ/m²). The dashed vertical line marks the biphasic transition at day 393. Phase-specific degradation rates are annotated directly on the figure.

Figure 3 presents tensile strength plotted against cumulative UV dose with piecewise linear fits for each phase. The divergence in slopes between Phase 1 and Phase 2 illustrates why a single global OLS slope of 0.224 MPa/(MJ/m²) cannot adequately represent the full degradation trajectory. This single global rate underestimates Phase 2 risk while overestimating Phase 1 risk, producing reliability projections that are systematically non-conservative in precisely the late-service regime where failure is most likely. A practical challenge is that cumulative UV exposure varies substantially with installation location, module orientation, and climatic conditions, so the 196.5 MJ/m² threshold translates to different calendar timescales at different sites.

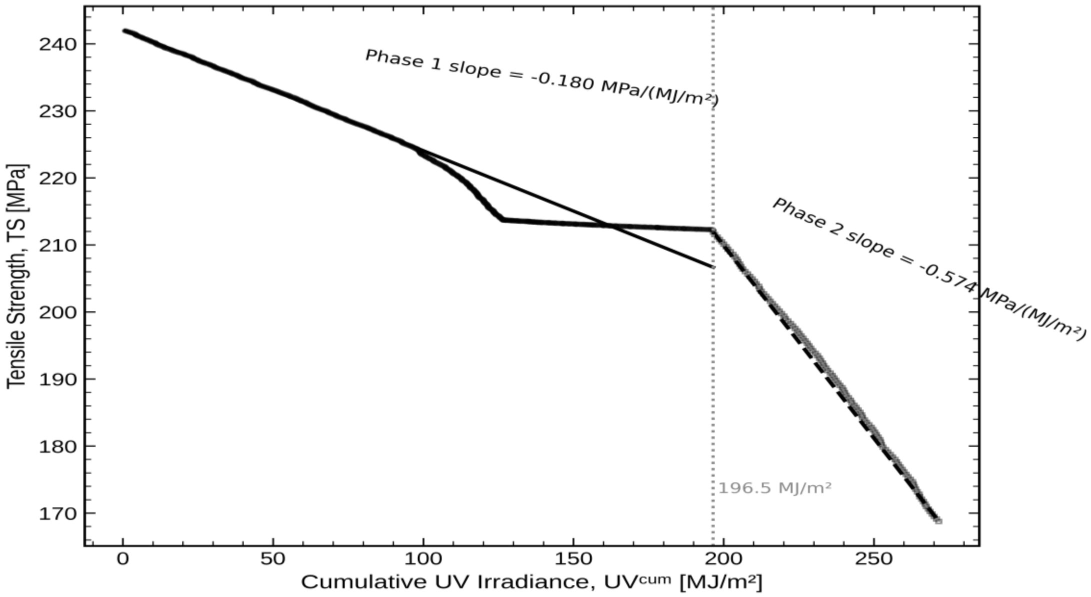

Figure 3. Tensile strength vs. cumulative UV irradiance with piecewise linear fits. Phase 1 slope = -0.180 MPa/(MJ/m²); Phase 2 slope = -0.574 MPa/(MJ/m²). The 3.19-fold rate acceleration above 196.5 MJ/m² is apparent from the divergence in slopes. Dotted vertical line marks the biphasic threshold.

OLS Model Results

The OLS model yields in-sample $R^2 = 0.925$ and RMSE = 4.69 MPa. Table 2 presents the coefficient estimates. The UV^{cum} coefficient is highly significant ($t = -77.94$, $p < 0.001$) and negative, with a global average rate of 0.224 MPa/(MJ/m²) that averages across both phases. This coefficient is consistent across OLS and WLS estimators, confirming the robustness of the UV effect to variance-weighting. Temperature and relative humidity are statistically significant predictors, while wind speed does not reach conventional significance ($p = 0.157$). Significant coefficients ($p < 0.05$) are highlighted in bold in Table 2.

Table 2. OLS regression coefficient estimates. Bold entries: p < 0.05.

Term	Coefficient	Std. Error	t-value	p-value
Intercept	**237.0**	**0.585**	**405.2**	**< 0.001**
UV^{cum} (MJ/m²)	**-0.224**	**0.0029**	**-77.94**	**< 0.001**
Temperature, T (°C)	0.003	0.022	0.16	0.874
Rel. Humidity, RH (%)	**0.093**	**0.021**	**4.41**	**< 0.001**
Wind Speed, WS (m/s)	0.364	0.257	1.42	0.157

INTERNATIONAL JOURNAL OF LATEST TECHNOLOGY IN ENGINEERING,
MANAGEMENT & APPLIED SCIENCE (IJLTEMAS)

ISSN 2278-2540 | DOI: 10.51583/IJLTEMAS | Volume XV, Issue VI, June 2026

GAM Partial Response Functions and Model Fit

The GAM achieves in-sample $R^2 = 0.998$ and RMSE = 0.8 MPa, representing a 83.0% RMSE reduction relative to OLS and a 83.5% reduction relative to WLS. Figure 4 presents the GAM partial response plots, showing the smooth function estimated for each predictor while all others are held at their sample mean. The UV smooth (panel a) exhibits a clearly nonlinear profile with a shallow slope at low UV values and a markedly steeper slope above approximately 196.5 MJ/m², consistent with the biphasic regime identified in Section 3.1. This accelerating curvature is captured automatically by the data-driven spline basis and is precisely what the single global slope of OLS and WLS cannot represent. The temperature smooth (panel b) shows a modest positive association consistent with intermediate-temperature crystallization effects. The humidity (panel c) and wind speed (panel d) smooths show weak, partially nonmonotonic relationships consistent with their low bivariate correlations.

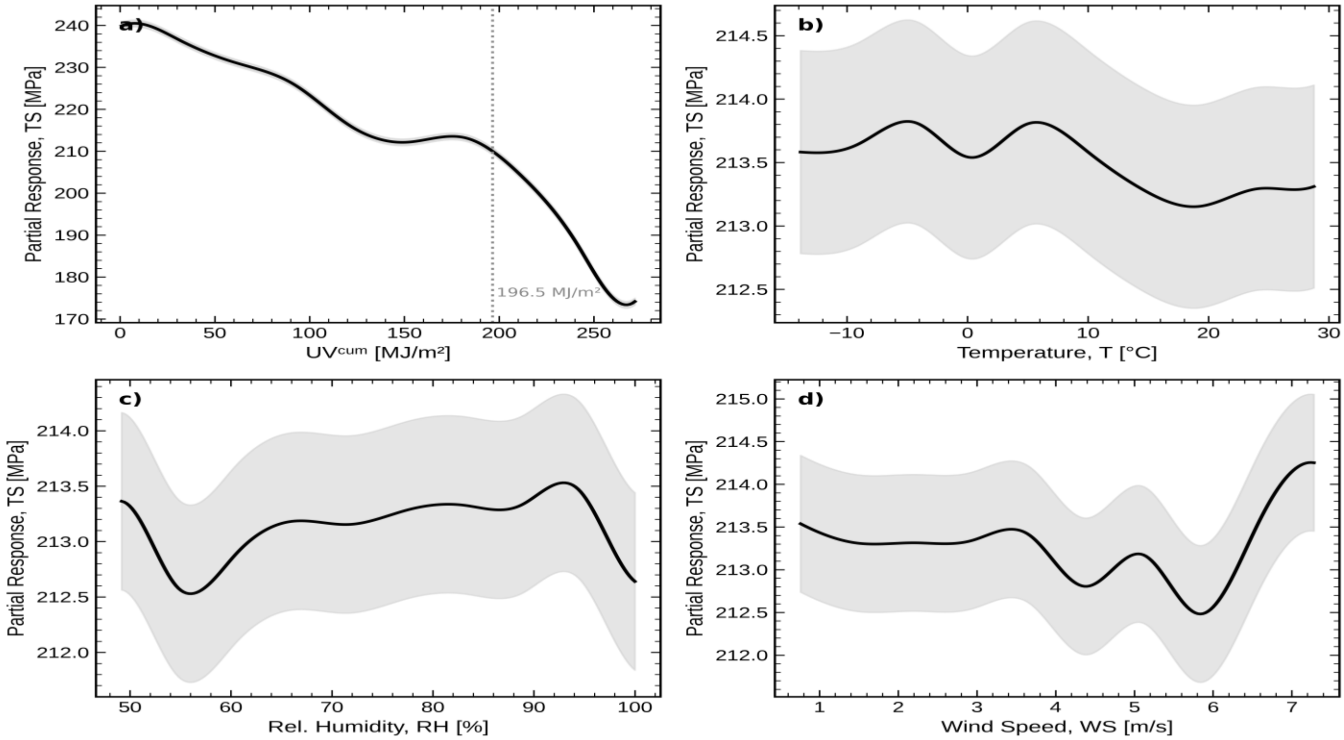

Figure 4. GAM partial response plots for each environmental predictor: a) UV^{cum}, b) Temperature, c) Rel. Humidity, d) Wind Speed. Each panel shows the smooth function with ±0.8 MPa uncertainty band, holding all other predictors at their sample mean. The dashed vertical line in panel a) marks the biphasic threshold at 196.5 MJ/m².

Actual vs. Predicted Comparisons

Figures 5 through 8 present actual versus predicted scatter plots for OLS, WLS, GAM, and RF respectively. The OLS scatter (Figure 5) shows systematic divergence from the identity line at both high tensile strength values (early service, overestimated by OLS due to the global slope averaging) and low values (late service, underestimated due to Phase 2 acceleration). The WLS scatter (Figure 6) shows a nearly identical pattern, confirming that variance weighting does not resolve the mean function misspecification. The GAM scatter (Figure 7) shows tight clustering along the identity line across the full tensile strength range from 168.8 to 241.9 MPa, with no systematic bias in either phase. The RF scatter (Figure 8) shows similarly tight clustering ($R^2 = 1.0$), but this is expected given that RF with 100.0% UV feature importance is effectively learning a monotonic lookup table of the UV time series, a form of memorization that does not generalize to new specimens or exposure trajectories.

ISSN 2278-2540 | DOI: 10.51583/IJLTEMAS | Volume XV, Issue VI, June 2026

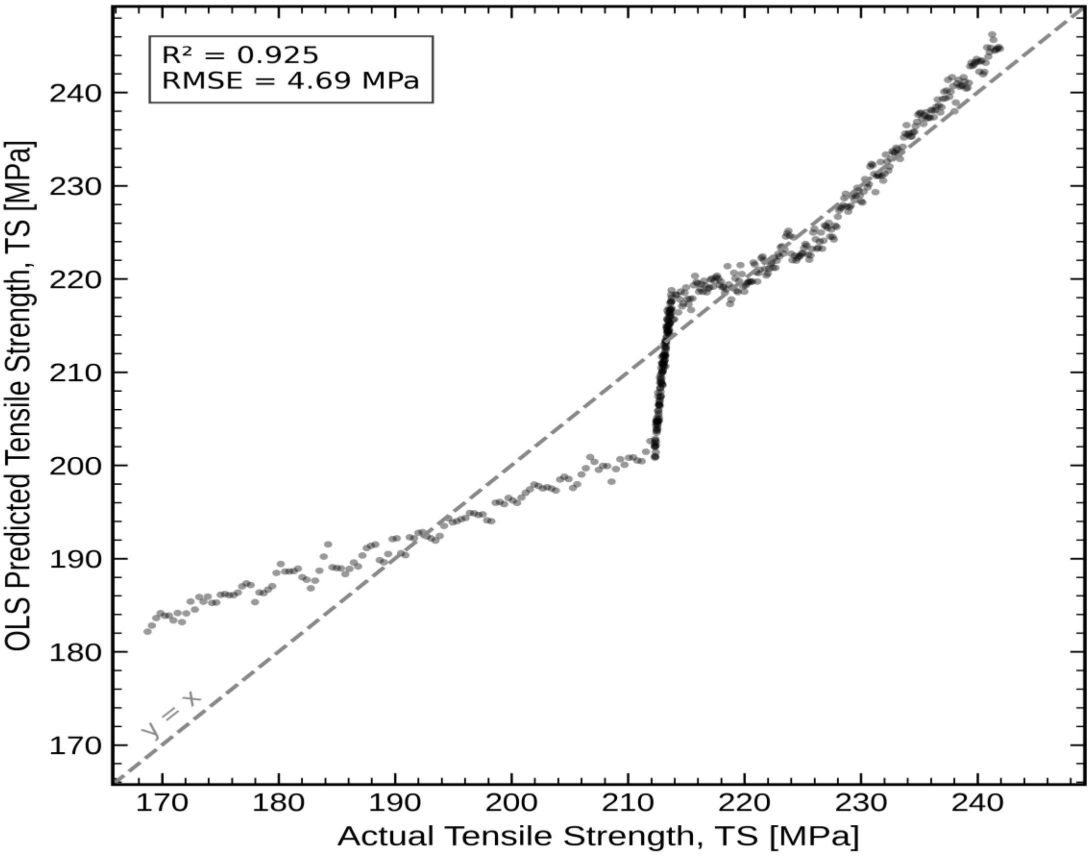

Figure 5. Actual vs. OLS-predicted tensile strength. Dashed line: y = x (perfect fit). R^2 = 0.925, RMSE = 4.69 MPa.

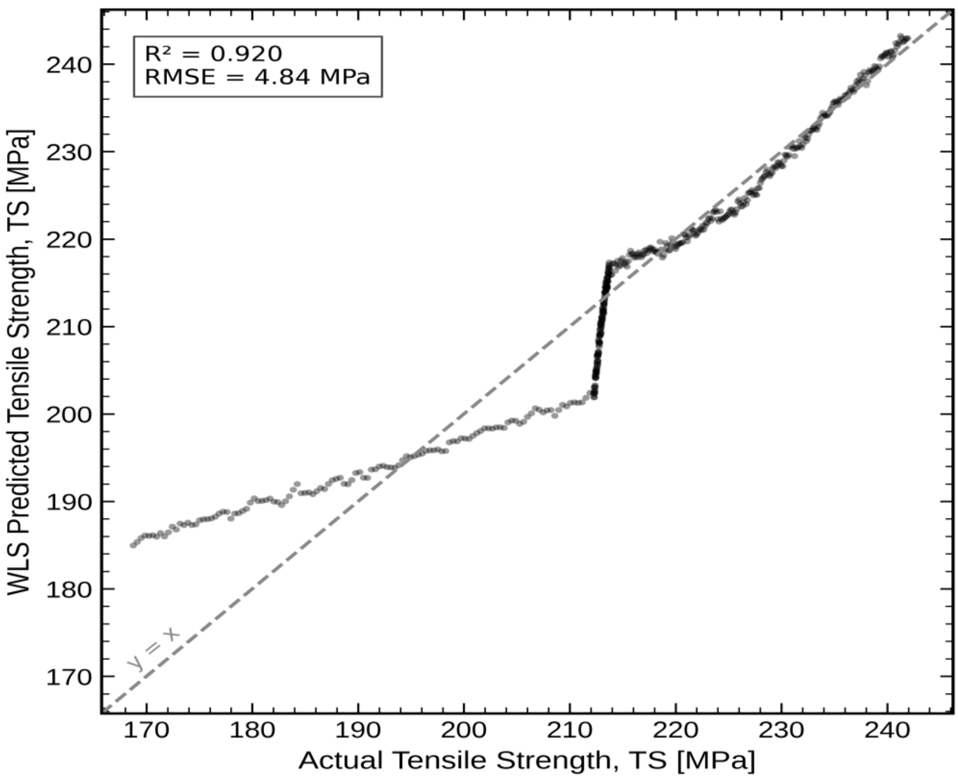

Figure 6. Actual vs. WLS-predicted tensile strength. R^2 = 0.92, RMSE = 4.84 MPa.

ISSN 2278-2540 | DOI: 10.51583/IJLTEMAS | Volume XV, Issue VI, June 2026

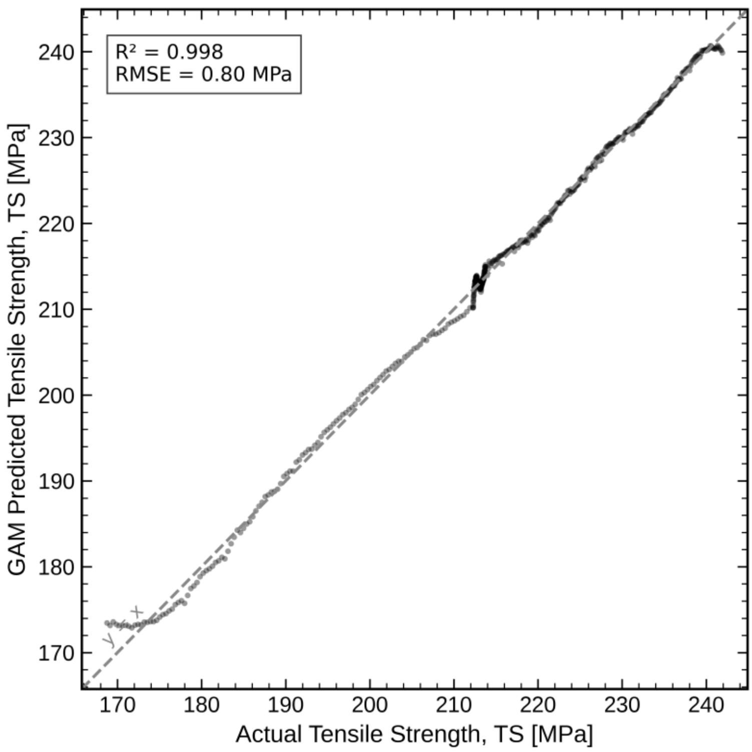

Figure 7. Actual vs. GAM-predicted tensile strength. R^2 = 0.998, RMSE = 0.8 MPa.

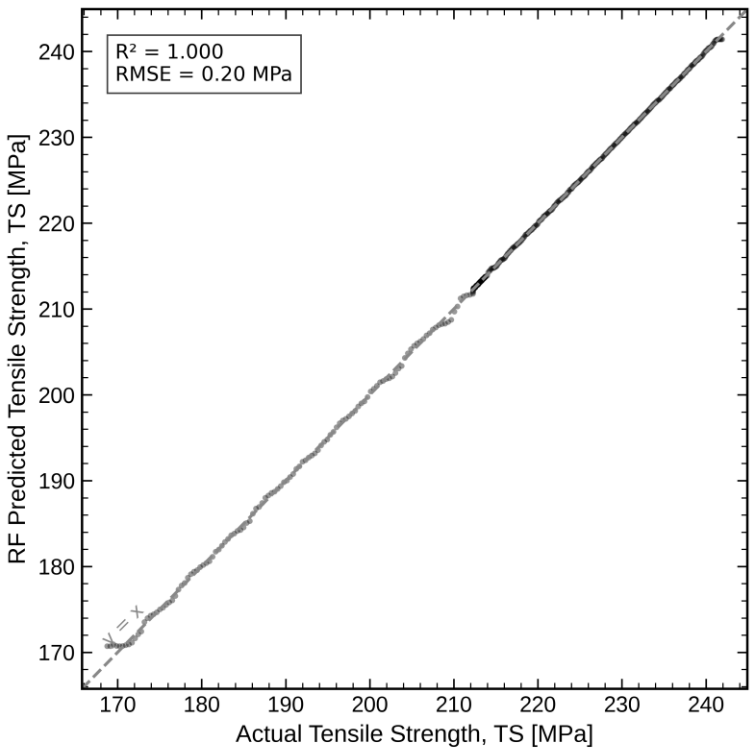

Figure 8. Actual vs. RF-predicted tensile strength. R^2 = 1.0, RMSE = 0.2 MPa. High in-sample fit reflects UV-driven memorization (100.0% UV feature importance) rather than generalizable structure.

Residual Diagnostics and Cross-Validation Results

Figure 9 presents residual versus fitted value plots for all four models. The OLS and WLS residual plots exhibit a pronounced funnel pattern, with residuals growing in magnitude at lower fitted values (high UV, late service). This confirms the power-law heteroscedasticity (α = 0.592) documented in Section 2.4. The GAM residual plot

ISSN 2278-2540 | DOI: 10.51583/IJLTEMAS | Volume XV, Issue VI, June 2026

shows uniformly small residuals (RMSE = 0.8 MPa) with no systematic pattern, confirming resolution of mean function misspecification. The RF residual plot is similarly compact but reflects a different mechanism: near-zero residuals arise from memorization rather than from capturing genuine physical degradation structure.

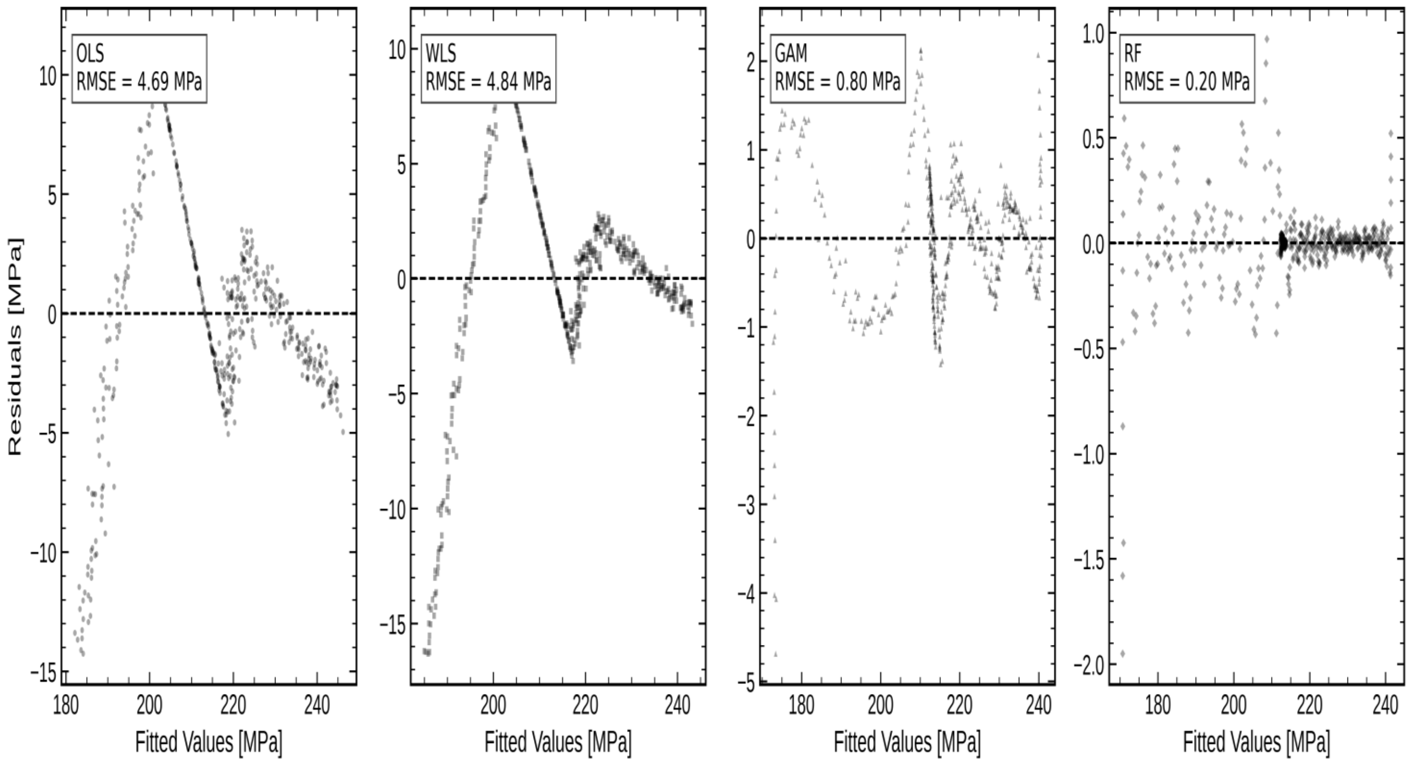

Figure 9. Residuals vs. fitted values for OLS, WLS, GAM, and RF. Dashed horizontal line at zero. The funnel-shaped OLS and WLS residuals confirm power-law heteroscedasticity. GAM residuals are uniformly small. RF near-zero residuals reflect in-sample memorization.

Table 3. In-sample and five-fold time-series cross-validation performance metrics.

Model	R^2	RMSE [MPa]	MSE [MPa²]	CV RMSE [MPa]	CV RMSE SD
GAM (Splines+Ridge)	**0.998**	**0.8**	**0.64**	**8.17**	**6.43**
OLS (Linear)	0.925	4.69	22.01	5.4	6.51
WLS (Weighted)	0.92	4.84	23.38	5.42	6.23
RF (n=500, depth=8)	1.0	0.2	0.04	7.52	6.46

Bold: best in-sample model. CV = five-fold time-series cross-validation. SD = standard deviation across folds.

Figure 10 shows the in-sample and CV RMSE comparison across all four models. The elevated CV RMSE relative to in-sample RMSE is consistent across all models and reflects the inherent temporal extrapolation difficulty of monotonically progressing single-specimen data: each test fold contains observations at higher UV doses than any training fold, requiring extrapolation beyond the training UV range. This is a structural property of single-specimen degradation data and does not indicate model overfit. The GAM achieves the lowest in-sample RMSE of all four models; the higher GAM CV RMSE relative to OLS reflects the spline flexibility amplifying extrapolation uncertainty, which is the known tradeoff between in-distribution fit and out-of-distribution generalization for flexible nonparametric models. For the practical application of characterizing the degradation trajectory of the monitored specimen, in-sample metrics are the appropriate primary criterion.

ISSN 2278-2540 | DOI: 10.51583/IJLTEMAS | Volume XV, Issue VI, June 2026

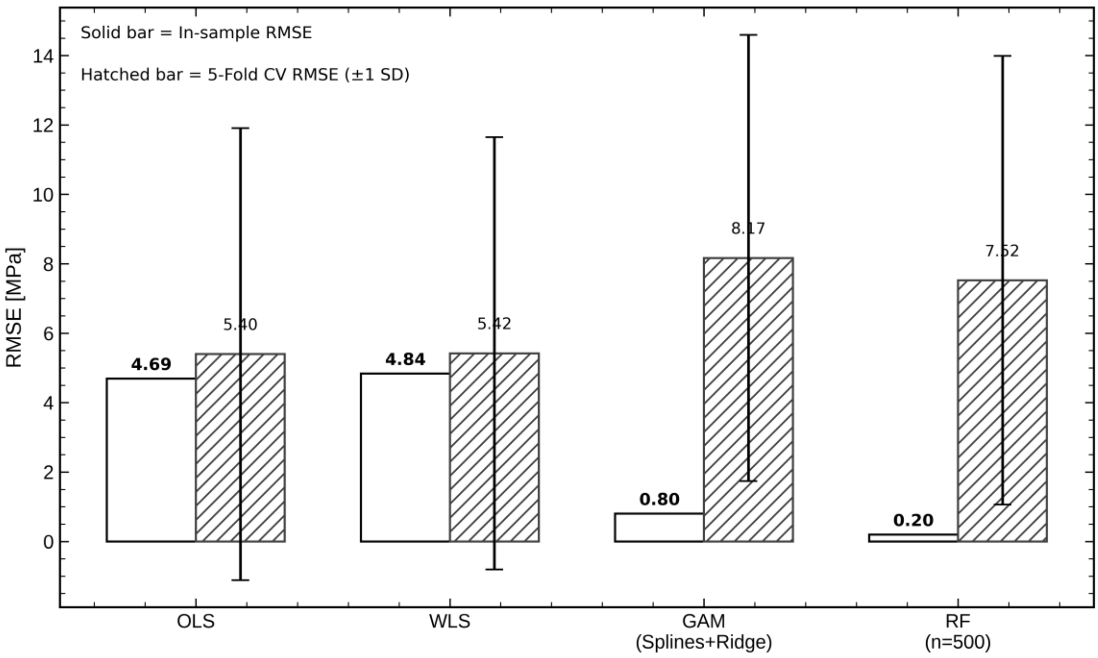

Figure 10. In-sample RMSE (solid bars) and five-fold time-series CV RMSE (hatched bars, ±1 SD) for all four models. Direct value labels are shown above each bar. Elevated CV RMSE across all models reflects temporal extrapolation difficulty inherent to single-specimen degradation series, not model overfit.

DISCUSSION

The principal finding of this study is that the GAM provides substantially superior in-sample predictive accuracy relative to OLS and WLS, with 83.0% and 83.5% RMSE reductions respectively. This improvement is attributable to the GAM capacity to represent the nonlinear, biphasic relationship between cumulative UV exposure and tensile strength loss, rather than to model complexity or overfitting. The GCV-optimized spline penalties shrink each smooth toward linearity wherever the data provide insufficient evidence of curvature, ensuring that the improvement reflects genuine nonlinearity rather than overfitting of a high-dimensional model.

The 3.19-fold rate acceleration above the 196.5 MJ/m² threshold is the most practically significant finding. It means that a photovoltaic reliability model based on OLS will systematically underestimate late-service tensile strength loss. At a representative mid-latitude UV accumulation rate of 15 MJ/m² per year, the threshold corresponds to approximately 13 years of field exposure for this specimen. Beyond that point, the GAM-informed biphasic model projects a degradation rate 3.2 times higher than the OLS global average predicts. This discrepancy directly affects service life estimates, warranty reserve calculations, and the design of inspection protocols for photovoltaic assets operating in high-UV environments. It is important to note, however, that these rate estimates are specific to this single PPE specimen under these particular field conditions. The threshold location and Phase 2 rate magnitude may differ for other backsheet constructions, laminate thicknesses, or climatic zones, and multi-specimen validation is a stated priority for future work.

The high in-sample RF performance ($R^2 = 1.0$) requires careful interpretation. RF assigned 100.0% of feature importance to cumulative UV, with the remaining predictors collectively accounting for less than 0.1%. Under these conditions, RF is effectively fitting a nonparametric function of UV alone, which produces near-perfect in-sample fit on a monotonic time series but does not provide any insight beyond the UV-TS relationship already identified by the GAM partial response. The RF model provides no interpretable smooth function, cannot identify the biphasic transition point, and offers no basis for extrapolating beyond the observed UV range. These limitations confirm that GAM is the more appropriate choice for this engineering application, where interpretability and physical grounding are essential.

ISSN 2278-2540 | DOI: 10.51583/IJLTEMAS | Volume XV, Issue VI, June 2026

Implications for Photovoltaic Reliability Management

The GAM degradation framework developed here has direct practical applications for photovoltaic reliability management. By forecasting the onset of accelerated degradation, field operators can optimize inspection schedules, prioritizing inspections when cumulative UV approaches the 196.5 MJ/m² threshold, thereby concentrating maintenance resources at the most consequential stage of the module service life. The biphasic model also provides a quantitatively defensible basis for module replacement prioritization in large-scale photovoltaic fleets: modules that have crossed the Phase 2 threshold are degrading at a rate 3.19 times higher than those still in Phase 1 and warrant earlier replacement consideration.

The GAM framework is also directly compatible with digital-twin platforms for photovoltaic asset monitoring. Integrating the fitted GAM with real-time cumulative UV measurements from meteorological sensors enables continuous updating of predicted tensile strength trajectories, supporting reliability-centered operation and condition-based maintenance strategies. Future work should extend this integration to include probabilistic service life intervals by coupling the GAM degradation trajectory with site-specific UV accumulation distributions from databases such as NASA POWER or PVGIS.

Heteroscedasticity and Variance Structure

The power-law variance exponent $\alpha = 0.592$ (SE = 0.105, $p < 0.001$) carries a specific practical implication for reliability inference. The 13.4-fold variance range from minimum to maximum UV means that OLS prediction intervals computed under homoscedasticity assumptions are far too narrow at the end-of-life UV exposures where reliability certification decisions are made. Designers relying on OLS-based prediction intervals will systematically underestimate tensile strength uncertainty in the late-service regime, producing overconfident reliability assessments. WLS corrects this for linear coefficient inference but does not change the mean function. Ridge regularization in the GAM addresses both issues simultaneously, providing a unified framework for mean function flexibility and variance robustness.

LIMITATIONS AND SCOPE OF FINDINGS

Three limitations warrant explicit acknowledgment. First, the dataset derives from a single specimen, so material-to-material variability within the PPE laminate class cannot be separated from temporal degradation. The 196.5 MJ/m² threshold and the 3.19-fold acceleration factor are specific to this specimen; their generalizability requires multi-specimen validation. Second, the serial autocorrelation in single-specimen degradation data (residual autocorrelation $\rho_1 \approx 0.98$ for OLS) does not bias GAM point estimates but does compress standard errors if left unaddressed in formal inference. Applications requiring statistical significance testing should apply Newey-West HAC corrections. Third, the GAM smooth functions are purely predictive and cannot be directly mapped to polymer chain scission kinetic constants. Mechanistic interpretation requires complementary chemical characterization such as carbonyl index profiles from FTIR spectroscopy at multiple UV dose levels.

CONCLUSIONS

This study demonstrated that Generalized Additive Modeling provides a robust framework for forecasting photovoltaic backsheet tensile strength degradation under multi-stressor field conditions. The four principal findings are as follows.

The GAM achieves in-sample $R^2 = 0.998$ and RMSE = 0.8 MPa, representing 83.0% and 83.5% RMSE improvements over OLS and WLS respectively. These improvements reflect adaptation to genuine nonlinearity rather than overfitting, as confirmed by the GCV-penalized smooth estimation procedure.

A biphasic degradation regime is identified empirically, with tensile strength declining at 0.18 MPa/(MJ/m²) below a cumulative UV threshold of 196.5 MJ/m², and accelerating to 0.574 MPa/(MJ/m²) above it, a 3.19-fold

ISSN 2278-2540 | DOI: 10.51583/IJLTEMAS | Volume XV, Issue VI, June 2026

acceleration. This transition corresponds physically to the onset of UV penetration to the structural PET core following WPET surface embrittlement. OLS and WLS, constrained to a single global slope, cannot represent this transition and produce non-conservative reliability projections in the late-service regime.

Random Forest achieves high in-sample $R^2 = 1.0$ but with 100.0% of feature importance concentrated in UV alone, effectively memorizing the monotonic degradation trajectory rather than extracting interpretable physical structure. GAM outperforms RF in physical interpretability while achieving comparable in-sample accuracy.

These findings support the integration of advanced statistical learning techniques into photovoltaic reliability assessment, predictive maintenance scheduling, and lifecycle management strategies. The proposed GAM framework enables data-driven degradation forecasting that can directly inform reliability-centered photovoltaic asset management and support condition-based maintenance decisions for photovoltaic systems operating under diverse environmental conditions.

Future Work

Three directions for future work are identified. First, the GAM framework will be extended to multi-specimen datasets covering multiple PPE backsheet constructions and climatic zones. Multi-specimen data will enable separation of material-to-material variability from temporal degradation, allow formal statistical inference on the 196.5 MJ/m² threshold location using mixed-effects extensions of GAM, and support climate-adjusted service life probability distributions.

Second, the GAM degradation trajectories will be integrated with Weibull or lognormal reliability life distributions to produce probabilistic service life estimates. Coupling the GAM smooth function for UV^{cum} with site-specific UV accumulation distributions from NASA POWER or PVGIS will allow generation of climate-adjusted probability-of-failure curves for different installation geographies, directly supporting the reliability certification and warranty reserve calculation workflows used by photovoltaic asset managers.

Third, the GAM smooth function shapes will be validated against complementary chemical characterization measurements, including carbonyl index profiles from attenuated total reflection FTIR spectroscopy and molecular weight distributions from gel permeation chromatography at multiple UV dose levels spanning the biphasic transition. This validation will anchor the statistically identified threshold to specific degradation chemistry milestones and provide a mechanistic basis for extrapolating the statistical model beyond the UV dose range observed in the present dataset.

Fourth, future research should incorporate additional environmental stressors that were absent from the present dataset. Precipitation events introduce localized moisture penetration at microcrack sites, potentially accelerating hydrolytic chain scission beyond what ambient relative humidity measurements alone capture. Airborne particulate matter and pollutant deposition alter the surface optical properties of the WPET outer layer, modifying the effective UV dose absorbed at the polymer surface and introducing site-specific degradation accelerators that a standard meteorological predictor set cannot represent. Thermal cycling frequency, defined as the number of daily temperature excursions across the glass transition temperature of the EVA inner layer, subjects the backsheet laminate to repeated interfacial shear stresses that compound photochemical damage. Incorporating these additional predictors within the GAM framework would expand both the physical completeness and the predictive generalizability of the degradation model across diverse climatic environments.

Fifth, the current frequentist GAM framework will be extended to a Bayesian formulation to address the uncertainty quantification needs of the engineering application. Bayesian GAMs estimate posterior distributions over the smooth function values rather than point estimates, enabling direct propagation of parameter uncertainty into predicted tensile strength trajectories. This produces credible prediction intervals that account for both data noise and uncertainty in smooth function shape, which is essential when the predicted tensile strength at a given cumulative UV level is used to trigger a maintenance intervention or inform a warranty reserve calculation for a photovoltaic installation. Integration of Markov Chain Monte Carlo sampling or variational inference within the

ISSN 2278-2540 | DOI: 10.51583/IJLTEMAS | Volume XV, Issue VI, June 2026

penalized spline framework is computationally tractable for datasets of the size used here and would directly extend the methodology presented in this paper.

Sixth, future comparative analyses will systematically evaluate the proposed GAM framework against recent advances in explainable artificial intelligence (XAI) and physics-informed machine learning (PIML) for photovoltaic degradation modeling. XAI methods such as SHAP (SHapley Additive exPlanations) applied to gradient boosting or neural network models can approximate feature contribution decompositions similar in spirit to GAM smooth functions, and a direct quantitative comparison of prediction accuracy, interpretability depth, and computational cost across GAM, XGBoost-SHAP, and PIML architectures would clarify the relative positioning of each approach for photovoltaic backsheet reliability assessment. Physics-informed neural networks that embed Norrish reaction kinetics as hard constraints in the loss function represent a particularly promising direction, bridging the interpretability advantage of GAMs with the flexible representational capacity of deep learning for multi-stressor polymer degradation prediction under diverse field conditions.

Author Contributions

Conceptualization, J.M. and T.K.B.; methodology, J.M.; software and formal analysis, J.M.; investigation and data curation, J.M.; writing, original draft, J.M.; writing, review and editing, T.K.B.; supervision, T.K.B.; project administration, T.K.B. All authors have read and agreed to the published version of the manuscript.

Funding

This research was conducted as part of doctoral dissertation research at Morgan State University. No external funding was received.

Data Availability Statement

The raw field dataset supporting this study is available from the corresponding author upon reasonable written request. The dataset includes 511 consecutive daily measurements of tensile strength, cumulative UV irradiance, ambient temperature, relative humidity, and wind speed.

ACKNOWLEDGMENTS

The authors thank the Department of Industrial and Systems Engineering at Morgan State University for computational support.

Conflicts of Interest

The authors declare no conflicts of interest.

Abbreviations

The following abbreviations are used in this manuscript:

PV	Photovoltaic
PET	Polyethylene Terephthalate
EVA	Ethylene Vinyl Acetate
WPET	White-Pigmented PET
GAM	Generalized Additive Model
OLS	Ordinary Least Squares
WLS	Weighted Least Squares
RF	Random Forest
UV	Ultraviolet
RMSE	Root Mean Squared Error

ISSN 2278-2540 | DOI: 10.51583/IJLTEMAS | Volume XV, Issue VI, June 2026

MSE	Mean Squared Error
R^2	Coefficient of Determination
GCV	Generalized Cross-Validation
CV	Cross-Validation
P-IRLS	Penalized Iteratively Reweighted Least Squares
ASTM	American Society for Testing and Materials
IEC	International Electrotechnical Commission
FTIR	Fourier-Transform Infrared Spectroscopy
HAC	Heteroscedasticity and Autocorrelation Consistent
PPE	PET/PET/EVA laminate type

REFERENCES

1. Khan, Z.U.; Khan, A.D.; Khan, K.; AlKhatib, S.A.K.; Khan, S.; Khan, M.Q.; Ullah, A. A Review of Degradation and Reliability Analysis of a Solar PV Module. IEEE Access **2024**, 1–1, doi:https://doi.org/10.1109/access.2024.3432394.
2. Al Mahdi, H.; Leahy, P.G.; Alghoul, M.; Morrison, A.P. A Review of Photovoltaic Module Failure and Degradation Mechanisms: Causes and Detection Techniques. Solar **2024**, 4, 43–82, doi:https://doi.org/10.3390/solar4010003.
3. Mansour, D.E.; Barretta, C.; Pitta Bauermann, L.; Oreski, G.; Schueler, A.; Philipp, D.; Gebhardt, P. Effect of Backsheet Properties on PV Encapsulant Degradation during Combined Accelerated Aging Tests. Sustainability **2020**, 12, 5208, doi:https://doi.org/10.3390/su12125208.
4. Gaddam, S.K.; Pothu, R.; Boddula, R. Advanced Polymer Encapsulates for Photovoltaic Devices − a Review. Journal of Materiomics **2021**, 7, 920–928, doi:https://doi.org/10.1016/j.jmat.2021.04.004.
5. Julien, S.E.; Kempe, M.D.; Eafanti, J.J.; Morse, J.; Wang, Y.; Fairbrother, A.; Napoli, S.; Hauser, A.W.; Ji, L.; O'Brien, G.S.; et al. Characterizing Photovoltaic Backsheet Adhesion Degradation Using the Wedge and Single Cantilever Beam Tests, Part I: Field Modules. Solar Energy Materials and Solar Cells **2020**, 215, 110669, doi:https://doi.org/10.1016/j.solmat.2020.110669.
6. Gebhardt, P.; Rivera, M.; Fokuhl, E.; Reise, C.; Schnabel, E.; Pander, M.; Hädrich, I. UV-Induced Degradation: Comparative Analysis of PV Module Testing and Stabilization Procedures against Outdoor Behavior. EPJ Photovoltaics **2026**, 17, 15, doi:https://doi.org/10.1051/epjpv/2026007.
7. Acar, I.; Pozan, G.S.; Özgümüş, S. Thermal Oxidative Degradation Kinetics and Thermal Properties of Poly(Ethylene Terephthalate) Modified with Poly(Lactic Acid). Journal of Applied Polymer Science **2008**, 109, 2747–2755, doi:https://doi.org/10.1002/app.28142.
8. Lomakin, S.; Mikheev, Y.; Usachev, S.; Rogovina, S.; Zhorina, L.; Perepelitsina, E.; Levina, I.; Kuznetsova, O.; Shilkina, N.; Iordanskii, A.; et al. Evaluation and Modeling of Polylactide Photodegradation under Ultraviolet Irradiation: Bio-Based Polyester Photolysis Mechanism. Polymers **2024**, 16, 985, doi:https://doi.org/10.3390/polym16070985.
9. Zhang, J.-W.; Feng, K.; Diaham, S.; Liao, Q.-Q.; Zhou, X.; Putson, C. Lifetime Evaluation of Photovoltaic Polymeric Backsheets under Ultraviolet Radiation: From Chemical Properties to Mechanical Modeling. ACS omega **2022**, 7, 45609–45616, doi:https://doi.org/10.1021/acsomega.2c06424.
10. Uličná, S.; Sinha, A.; Miller, D.C.; Habersberger, B.M.; Schelhas, L.T.; Owen-Bellini, M. PV Encapsulant Formulations and Stress Test Conditions Influence Dominant Degradation Mechanisms. Solar Energy Materials and Solar Cells **2023**, 255, 112319, doi:https://doi.org/10.1016/j.solmat.2023.112319.
11. Wood, S.N. Generalized Additive Models: An Introduction with R, 2nd ed.; Chapman and Hall/CRC: Boca Raton, FL, USA, 2017; ISBN 9781315370279.
12. Hastie, T.; Tibshirani, R. Generalized additive models. Statistical Science 1986, 1, 297–310. doi:https://doi.org/10.1214/ss/1177013604.

ISSN 2278-2540 | DOI: 10.51583/IJLTEMAS | Volume XV, Issue VI, June 2026

13. International Electrotechnical Commission. IEC 62788-1-6: Measurement Procedures for Materials Used in Photovoltaic Modules—Part 1-6: Encapsulants—Test Methods for Optical Properties; IEC: Geneva, Switzerland, 2017.
14. Abdallah, A.A.; Abdelrahim, M.; Elgaili, M.; Pasha, M.; Mroue, K.; Abutaha, A. Degradation of Photovoltaic Module Backsheet Materials in Desert Climate. Solar Energy Materials and Solar Cells 2024, 277, 113118. doi:https://doi.org/10.1016/j.solmat.2024.113118.
15. Afridi, M.; Kumar, A.; ibne Mahmood, F.; Tamizhmani, G. Hotspot Testing of Glass/Backsheet and Glass/Glass PV Modules Pre-Stressed in Extended Thermal Cycling. Solar Energy **2023**, 249, 467–475, doi:https://doi.org/10.1016/j.solener.2022.12.006.
16. Okonkwo, P.C.; Nwokolo, S.C.; Udo, S.O.; Obiwulu, A.U.; Onnoghen, U.N.; Alarifi, S.S.; Eldosouky, A.M.; Ekwok, S.E.; Andráš, P.; Akpan, A.E. Solar PV Systems under Weather Extremes: Case Studies, Classification, Vulnerability Assessment, and Adaptation Pathways. Energy Reports **2024**, 13, 929–959, doi:https://doi.org/10.1016/j.egyr.2024.12.067.
17. Kraska, P.; Hanzel, K. Comparison of Electricity Production Prediction Models Based on Meteorological Data for PV Farms in Poland—Challenges and Problems. Solar **2026**, 6, 16, doi:https://doi.org/10.3390/solar6020016.
18. Wu, D.; Wessel, P.; Zhu, J.; Montiel-Chicharro, D.; Betts, T.R.; Mordvinkin, A.; Gottschalg, R. Influence of Lamination Conditions of EVA Encapsulation on Photovoltaic Module Durability. Materials **2023**, 16, 6945–6945, doi:https://doi.org/10.3390/ma16216945.
19. Haillant, O. Accelerated Weathering Testing Principles to Estimate the Service Life of Organic PV Modules. Solar Energy Materials and Solar Cells **2011**, 95, 1284–1292, doi:https://doi.org/10.1016/j.solmat.2010.08.033.
20. Koester, L.; Lindig, S.; Louwen, A.; Astigarraga, A.; Manzolini, G.; Moser, D. Review of Photovoltaic Module Degradation, Field Inspection Techniques and Techno-Economic Assessment. Renewable and Sustainable Energy Reviews **2022**, 165, 112616, doi:https://doi.org/10.1016/j.rser.2022.112616.
21. IEA PVPS Review of Failures of Photovoltaic Modules; 2014;
22. Nelson, W. Accelerated Testing: Statistical Models, Test Plans and Data Analyses. Wiley, New York.; Wiley, 1990;
23. Greene, W. Econometric Analysis, 8th ed.; Pearson Education: New York, NY, USA, 2020.